Amplitude-preserving wave-equation imaging

Paul Sava, James Rickett, Marie Prucha, and Biondo Biondi, Stanford University*

SUMMARY

We recover the amplitudes of the reflectivity function obtained by wave-equation migration by compensating for the amplitude distortions created by the imaging condition and by the incomplete reflector illumination. The amplitude effects produced by the imaging condition must be taken into account even for simple velocity models, and they are perfectly compensated by a diagonal scaling in the frequency domain. The effects produced by the incomplete reflector illumination must be taken into account in the presence of complex overburden and/or irregular recording geometries, and they are partially compensated using normalized migration or regularized inversion in the angle-domain.

INTRODUCTION

Migration is described by a linear operator which is the *adjoint* of a forward modeling operator (**F**) rather than its *inverse*. The implication is that, although migration treats kinematics correctly, the amplitudes of migrated images do not accurately represent seismic reflectivity. We can recover correct amplitudes using inversion instead of migration (Duquet and Marfurt, 1999; Ronen and Liner, 2000). However, the operator we try to invert (**F**) is only an approximation for the processes that govern wave propagation in the subsurface, since it is defined by approximate physics, limited recording geometry etc. Therefore, even if computational cost is not an issue, we cannot compute an exact inverse to our operator and have to retort to approximate inverses, typically in the ℓ_2 norm. Mathematically, we can relate the seismic data $\mathbf{d}$, to the migrated $\mathbf{m}$ and the inverted $\mathbf{m}_{\ell_2}$ images by the equations:

$$\mathbf{m}_{\ell_2} = \left(\mathbf{F}'\mathbf{F}\right)^{-1}\mathbf{F}'\mathbf{d} = \left(\mathbf{F}'\mathbf{F}\right)^{-1}\mathbf{m} \tag{1}$$

The following sections describe the various components of the amplitude preserving wave-equation imaging operator. We first address the issues related to amplitude compensation of the effects introduced by the imaging condition, and then we address the issues related to illumination, and propose normalized migration and regularized inversion techniques.

ANGLE-DOMAIN COMMON IMAGE GATHERS

Traditionally, migration velocity analysis and AVO employ offset-domain common-image gathers, since the relevant information is not described by the zero-offset images. However, it is difficult to produce these gathers with wave-equation migration because the offset dimension of the downward continued data shrinks with depth. A solution to this problem is to use angle-domain common image gathers (ADCIG) which describe the reflectivity as a function of incidence angle at the reflector.

Angle gathers can be conveniently formed in the frequency domain. Sava et al. (2001) show that we can describe ADCIGs in the image space, both in the spatial and Fourier domains, using the equations:

$$\tan\gamma = -\left.\frac{\partial z}{\partial h}\right|_{t,x}, \quad \tan\gamma = -\frac{k_h}{k_z}. \tag{2}$$

Equations (2) are derived in constant velocity media, but they remain perfectly valid in media with an arbitrary velocity if we consider h to be the effective offset at the reflector depth and not the surface offset (Figure 1). Wave-equation migration is ideally suited to compute angle gathers using such a method, since the migration output is precisely described by the offset at the reflector depth (a model parameter), and not by the surface offset (a data parameter).

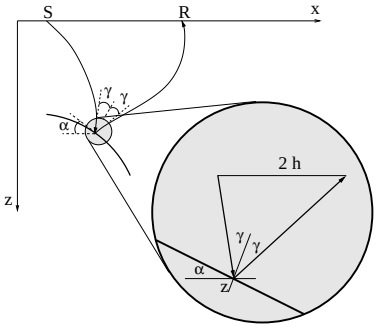

Figure 1: A scheme of reflection rays in arbitrary velocity media.

Similarly to Equations (2), we can compute ADCIG in the data space using the equations (Prucha et al., 1999)

$$p_h = \frac{\partial t}{\partial h}, \quad p_h = \frac{k_h}{\omega}. \tag{3}$$

Both Equations (2) and (3) can be used to compute image gathers through radial trace transforms in the Fourier domain.

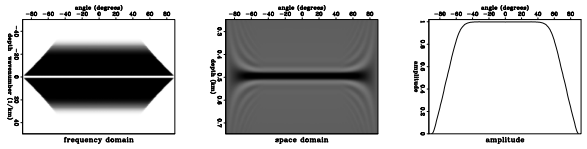

Figure 2: Angle gather created from an ideal offset gather.

AMPLITUDE-PRESERVING MIGRATION

Figure 2 shows a simple synthetic model consisting of a unique event perfectly focused at zero offset. In the angle-domain, we obtain a flat event of constant amplitude, but which decays at high angles because of the limited sampling of the offset axis (Sava et al., 2001).

Figures 3 and 4 show the angle gathers computed from images obtained by modeling followed by migration of the original synthetic image. Not surprisingly, since we have used the same velocity for both modeling and migration, the angle gathers are perfectly flat. However, the amplitude response is far from what we expect: neither ADCIG method produces constant amplitudes The explanation is that we have applied a succession of the forward (modeling) and adjoint (migration) of an incomplete linear operator which does not handle the amplitudes correctly.

We compensate the amplitudes using the weights introduced by the imaging step during migration, which in the $\omega - k$ domain are described by a diagonal operator representing the Jacobian of the transformation from the temporal frequency ω to the vertical wavenumber k_z ($d\omega/dk_z$). This Jacobian is different for the two methods of computing ADCIGs because the imaging is performed at constant offset ray parameter p_h (data space), and at constant offset wavenumber k_h (image space). For the image space method,

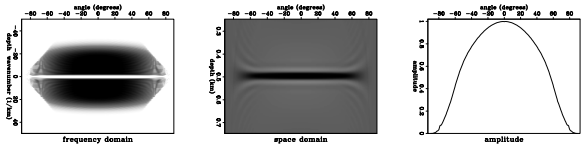

Figure 3: Image space ADCIG without amplitude correction.

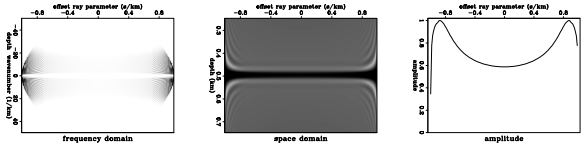

Figure 4: Data space ADCIG without amplitude correction.

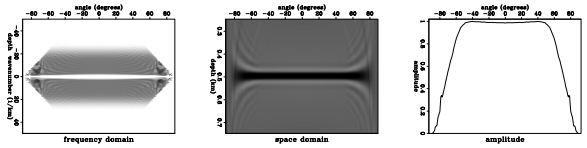

Figure 5: Image space ADCIG with amplitude correction.

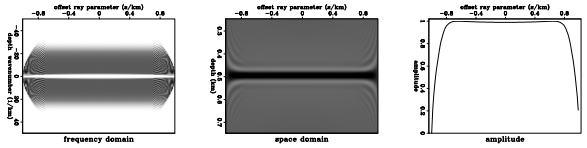

Figure 6: Data space ADCIG with amplitude correction.

the weighting function $\mathbf{W}_{k_h}$ is

$$\mathbf{W}_{k_h} = \left[s \left(\frac{\omega s}{k_{\rm zs}} + \frac{\omega s}{k_{\rm zr}} \right) \right]^{-1}, \tag{4}$$

while for the image space method, the Jacobian $\mathbf{W}_{p_h}$ is

$$\mathbf{W}_{p_h} = \left[\left(s - \frac{\mathbf{p_h} \cdot \mathbf{p_h}}{4s} \right) \left(\frac{\omega s}{k_{\rm zs}} + \frac{\omega s}{k_{\rm zr}} \right) + \frac{\mathbf{k_m} \cdot \mathbf{p_h}}{4\omega s} \left(\frac{\omega s}{k_{\rm zs}} - \frac{\omega s}{k_{\rm zr}} \right) \right]^{-1}, \tag{5}$$

where s is the local slowness, $k_{\rm zs}$ and $k_{\rm zr}$ are the vertical wavenumbers for the source and receiver components, and $\mathbf{k_m}$ is the midpoint wavenumber. Figures 5 and 6 show the amplitude-corrected ADCIGs.

Figure 7 shows an image gather computed for real data. The left panel is the gather computed without the Jacobian, while the right panel shows the gather with the Jacobian.

NORMALIZED MIGRATION

Rather than trying to solve the full inverse problem given by Equation (1), we can look for a diagonal operator $\mathbf{W}_{\rm m}$ such that

$$\mathbf{m}_{\ell_2} \approx \mathbf{W}_{\rm m}^2 \, \mathbf{F}' \mathbf{d} \tag{6}$$

Claerbout and Nichols (1994) noticed that if we model and remigrate a reference image, the ratio between the reference image and the modeled/remigrated image will be a weighting function with the correct physical units. For example, the weighting function, $\mathbf{W}_{\rm m}$, whose square is given by

$$\mathbf{W}_{\rm m}^2 = \frac{\mathbf{diag}\,(\mathbf{m}_{\rm ref})}{\mathbf{diag}\,(\mathbf{F}'\mathbf{F}\mathbf{m}_{\rm ref})} \approx \left(\mathbf{F}'\mathbf{F}\right)^{-1}, \tag{7}$$

will have the same units as $\mathbf{F}^{-1}$. Furthermore, $\mathbf{W}_{\rm m}^2$ will be the *ideal* weighting function if the reference model ($\mathbf{m}_{\rm ref}$) equals the true model and we have the correct modeling/migration operator.

However, since we do not know $\mathbf{m}_{\rm ref}$, we have to substitute an alternative model. Claerbout and Nichols (1994) attribute to Symes the idea of using the adjoint (migrated) image as the reference model. The rationale for this is that migration provides a robust estimate of the true model. A second alternative is a monochromatic reference image consisting of purely flat events. This is similar to the flat-event calibration proposed by Black and Schleicher (1989) for Kirchhoff DMO. Illumination calculated from this model is completely independent of the data.

The Amoco 2.5-D synthetic dataset provides an excellent test for the weighting functions discussed above. The velocity model contains significant structural complexity in the upper 3.8 km, and a flat reflector of uniform amplitude at about 3.9 km depth. The data were generated by 3-D acoustic finite-difference modeling of the 2.5-D velocity model. However, making the test more difficult is the fact that the 2-D linear one-way recursive extrapolators (Ristow and Ruhl, 1994) that we use for modeling and migration do not accurately predict the 3-D geometric spreading and multiple reflections that are present in this dataset.

Figure 8 compares the original migrated image [panel (a)] with the same image after modeling and remigration [panel (b)]. The weighting function derived from the ratio of panels (a) and (b) is shown in panel (c). Panel (d) shows the image obtained by modeling and remigrating a reference model consisting of purely flat events, and panel (e) shows the corresponding illumination-based weighting function. Finally panel (f) shows the result of normalizing the original migration [panel (a)] with the weighting function shown in panel (e).

For a quantitative comparison between images, we picked the maximum amplitude of the 3.9 km reflection event on the various images. The normalized standard deviation (NSD) of the reflector in the normalized images was 0.148 and 0.140 for the migrated and flat-layered reference models respectively, a significant improvement over 0.229 for the unnormalized image.

As it stands, the cost of computing a weighting function of this kind is twice the cost of a single migration. Add the cost of the migration itself, and this approach is 25% cheaper than running two iterations of conjugate gradients which costs two migrations per iteration.

However, the bandwidth of the weighting functions is much lower than that of the migrated images. This allows considerable computational savings, as modeling and remigrating a narrow frequency band around the central frequency produces similar weighting functions than the full bandwidth. Repeating the flat-event experiment with half the frequencies gives a NSD $= 0.147$ - the same as before within the limits of numerical error.

REGULARIZED INVERSION

Illumination problems generally occur in areas where the subsurface geology, and implicitly the wavefields, are complex. The angle-domain is particularly useful in such situations, because it avoids the artifacts that appear in offset-domain CIGs when multipathing occurs (Xu et al., 1998). However, reducing the artifacts caused by multipathing is not enough to overcome poor illumination, and we need to add additional constraints to our inversion scheme.

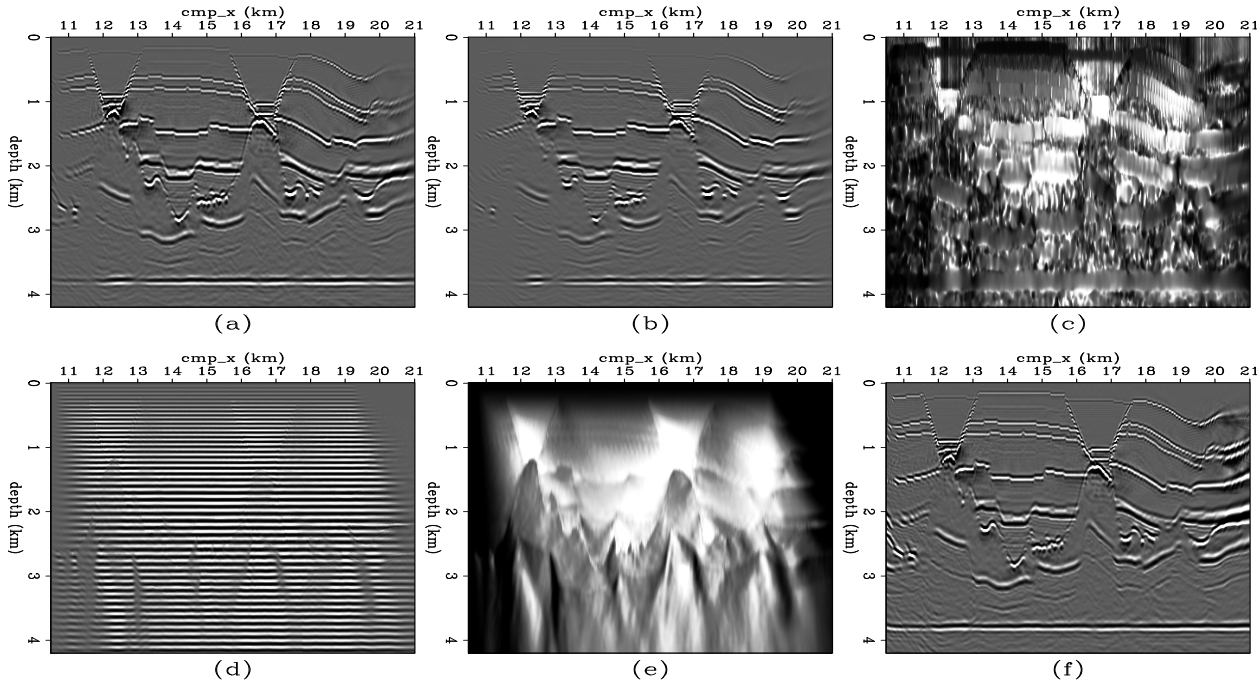

Figure 8: Demonstration of normalized wave-equation migration: (a) migrated image, (b) migrated image after modeling/remigration, (c) weights derived from panels (a) and (b), (d) flat-layered model after modeling/remigration, (e) weights derived from (d), and (f) image normalized by (e).

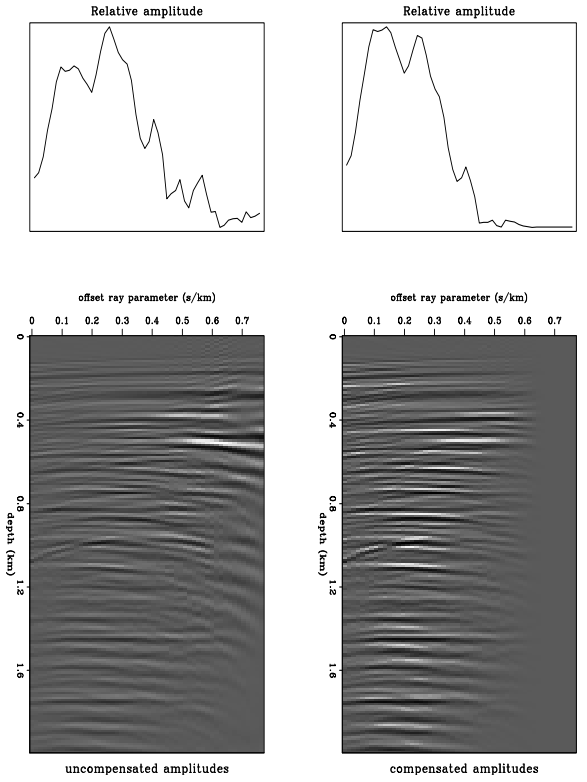

Figure 7: Real data example. The bottom panels are ADCIGs computed in the data space with (right) and without (left) amplitude compensation. The top panels represent the amplitude variation with p_h for an event at 1.75 km depth.

Our choice of inversion constraint is represented by dip penalty filters (Clapp et al., 1997) applied in the $p_h - z$ plane (Prucha et al., 2000). With these additional constraints, we can mathematically represent our inversion using two linear operators:

$$\begin{aligned} \mathbf{d} &\approx \mathbf{Fm} \\ 0 &\approx \mathbf{Am} \end{aligned} \tag{8}$$

where, as before, **d** and **m** are the data and model, respectively, **F** is the angle domain modeling operator described by Prucha et al. (1999), and **A** is the regularization operator. Increased convergence speed can be achieved using a change of variables that preconditions the model (Fomel et al., 1997). Our choice for the preconditioning operator is the inverse of the regularization operator ($\mathbf{A}^{-1}$), and so it acts as a smoothing operator along specified dips. Such operators fill-in the areas that do not contain real information, while smoothing and reducing the noise.

We applied the regularized inversion methodology to a synthetic 2-D dataset provided by the SMAART JV which is specifically designed to have serious illumination problems. A common p_h section from the migration of this dataset can be seen in Figure 9. The area of interest lies beneath the edge of the salt, where the amplitude of the reflectors decreases sharply (Figure 9). In addition, the salt edge is hardly visible in the cloud of noise surrounding it.

Figure 11 shows a common p_h section extracted from an image obtained after 5 iterations of regularized inversion, defined by Equation (8). We can see that the amplitude along the reflectors is more constant, and the reflectors can almost be traced all of the way to the salt. Furthermore, the noise under the salt is much weaker than in the migrated result, and the salt flank is sharper.

We also applied our regularized inversion methodology to a 2-D line from a 3-D North Sea dataset provided by TotalFinaElf. Figure 10 shows a constant p_h section extracted from the migrated

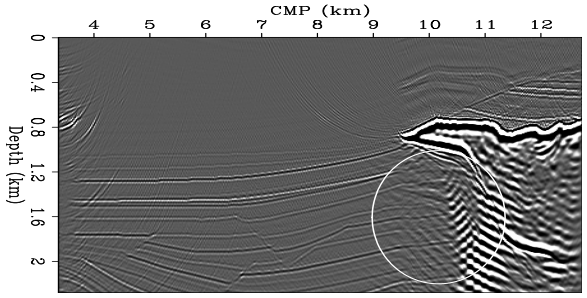

Figure 9: Synthetic data: migration (constant p_h).

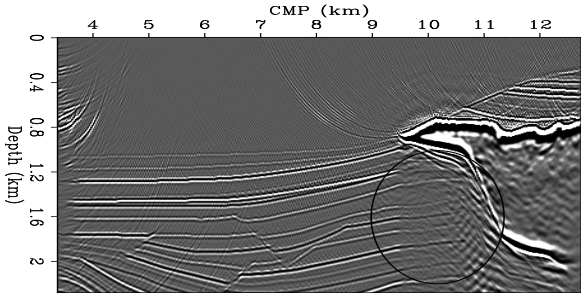

Figure 11: Synthetic data: regularized inversion (constant p_h).

image. Figure 12 shows a constant p_h section extracted from the image obtained after 5 iterations of regularized inversion. As expected, the signal-to-noise ratio has improved.

CONCLUSIONS

There are several aspects to producing reliable amplitudes via wave-equation migration schemes.

Firstly, we have discussed how to compensate for the conversion from temporal frequency to vertical wavenumber during imaging. For accurate AVA, this is necessary even for very simple velocity models.

Secondly, if lateral velocity variations are present in the earth, and/or the recording geometry is irregular, then seismic illumination at depth can vary. Again this may cause problems in amplitude interpretation.

We have shown that both normalized migration, and l_2 migration with appropriate regularization can help address illumination problems with wave-equation imaging.

ACKNOWLEDGEMENTS

We would like to thank BP, the SMAART JV and TotalFinaElf for providing us with the datasets used in this paper. We also thank the sponsors of the Stanford Exploration Project (SEP) for supporting the research presented in this paper. This research was also partially funded by the ACTI project # 4731U0015-3Q.

REFERENCES

Black, J. L., and Schleicher, K., 1989, Effect of irregular sampling on prestack DMO: 59th Annual Internat. Mtg., Soc. Expl. Geophys., Expanded Abstracts, 1144–1147.

Claerbout, J., and Nichols, D., 1994, Spectral preconditioning: SEP–**82**, 183–186.

Clapp, R. G., Fomel, S., and Claerbout, J., 1997, Solution steering with space-variant filters: SEP–**95**, 27–42.

Duquet, B., and Marfurt, K. J., 1999, Filtering coherent noise during prestack depth migration: Geophysics, **64**, no. 4, 1054–1066.

Fomel, S., Clapp, R., and Claerbout, J., 1997, Missing data interpolation by recursive filter preconditioning: SEP–**95**, 15–25.

Prucha, M., Biondi, B., and Symes, W., 1999, Angle-domain common-image gathers by wave-equation migration: 69th Ann. Internat. Meeting, Soc. Expl. Geophys., Expanded Abstracts, 824–827.

Prucha, M. L., Clapp, R. G., and Biondi, B., 2000, Seismic image regularization in the reflection angle domain: SEP–**103**, 109–119.

Ristow, D., and Ruhl, T., 1994, Fourier finite-difference migration: Geophysics, **59**, no. 12, 1882–1893.

Ronen, S., and Liner, C. L., 2000, Least-squares DMO and migration: Geophysics, **65**, no. 5, 1364–1371.

Sava, P., Biondi, B., and Fomel, S., 2001, Amplitude-preserved common image gathers by wave-equation migration: 71st Ann. Internat. Mtg., Soc. Expl. Geophys., Expanded Abstracts, submitted.

Xu, S., Chauris, H., Lambare, G., and Noble, M., 1998, Common angle image gather - A strategy for imaging complex media: 68th Annual Internat. Mtg., Society of Exploration Geophysicists, Expanded Abstracts, 1538–1541.

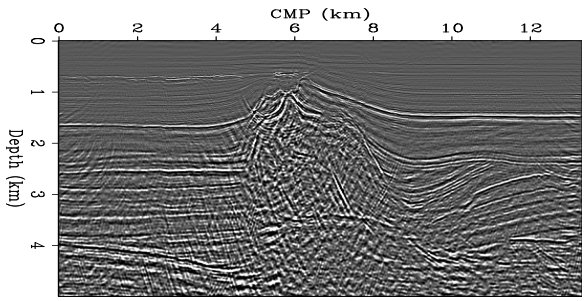

Figure 10: Real data: migration ($p_h = 0$).

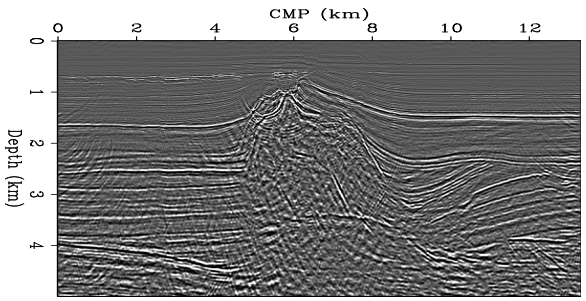

Figure 12: Real data: regularized inversion ($p_h = 0$).